Bulletin of Volcanology

Total grain size distribution of components of fallout deposits and implications for magma fragmentation mechanisms: examples from Campi Flegrei caldera (Italy)

--Manuscript Draft--

Manuscript Number:	BUVO-D-19-00080
Full Title:	Total grain size distribution of components of fallout deposits and implications for magma fragmentation mechanisms: examples from Campi Flegrei caldera (Italy)
Article Type:	Research Article
Corresponding Author:	Daniela Mele, Ph.D Università di Bari Bari, ITALY
Corresponding Author Secondary Information:	
Order of Authors:	Daniela Mele, Ph.D
	Antonio Costa
	Pierfrancesco Dellino
	Roberto Sulpizio
	Fabio Dioguardi
	Roberto Isaia
	Giovanni Macedonio
Funding Information:	
Abstract:	The knowledge of the Total Grain Size Distribution (TGSD) of the material erupted during explosive volcanic eruptions is one of the main factors for reducing uncertainty in quantitative hazard assessments and forecasts of tephra dispersal. A few TGSDs have been made available in the literature, mostly reconstructed by assuming that tephra deposits consisted of one single component. This simplification can introduce substantial bias in the interpretation of magma fragmentation mechanisms and significantly affect ash dispersion forecasts, since tephra actually include multiple components, such as juveniles, lithics, and crystals, each having a specific aerodynamic behaviour that depends on particle shape, density, and size. To investigate on this problem, in this study we reconstructed TGSDs by considering all components of the eruptive particle mixture. We focussed on the deposits of the Agnano Monte Spina, and Astroni eruptions, as to achieve a more robust quantitative hazard assessment of tephra fallout at Campi Flegrei (Italy). Field investigations and laboratory analyses on samples collected from proximal to distal locations allowed the input data to be obtained for the reconstruction of the TGSDs of juvenile, lithic, and crystal components by means of the Voronoi tessellation method. Results confirm that the bulk TGSD is the combination of the merging of different component subpopulations, each one with its weight. For the first time, this work shows how the systematic reconstruction of the TGSD with the presented method can give important information on magma fragmentation mechanisms, wall-rock erosion processes, and on the aerodynamic behaviour of each component at variable distances. Finally, the integration of data from distal tephra deposit allowed reassessing the erupted volumes of the eruptions considered in this research.
Suggested Reviewers:	Frances M. Beckett Met Office, Exeter, UK frances.beckett@metoffice.gov.uk
	Rosanna Bonasia Instituto Politecnico Nacional Escuela Superior de Ingenieria y Arquitectura Zacatenco rosannabonasia017@gmail.com
	James D.L. White Universita degli Studi di Palermo Dipartimento di Scienze della Terra e del Mare

	james.white@otago.ac.nz
	Bruce Houghton University of Hawal'I at Manoa bhought@soest.hawaii.edu
Author Comments:	Dear Editor, we wish to submit the manuscript entitled: "Total grain size distribution of components of fallout deposits and implications for magma fragmentation mechanisms: examples from Campi Flegrei caldera (Italy)" by Daniela Mele, Antonio Costa, Pierfrancesco Dellino, Roberto Sulpizio, Fabio Dioguardi, Roberto Isaia and Giovanni Macedonio, for your consideration for publication in Bulletin of Volcanology. The manuscript presents a novel approach for the quantification of the Total Grain Size Distribution (TGSD) of tephra generated during explosive eruptions, which discerns among the different components and sheds light on magma fragmentation processes, such as the control of bubble size distribution and wall rock erosion. Finally, the improved TGSD estimations of past explosive eruption at Campi Flegrei (Italy), have implications for tephra risk mitigation in the Neapolitan area. On behalf of the Authors Sincerely Daniela Mele

Total grain size distribution of components of fallout deposits and implications for magma fragmentation mechanisms: examples from Campi Flegrei caldera (Italy)

Mele D.[1], Costa A.[2], Dellino P. [1], Sulpizio R.[1,3], Dioguardi F.[4], Isaia R.[5], Macedonio G.[5]

[1] Dipartimento di Scienze della Terra e Geoambientali, Università degli Studi di Bari "Aldo Moro", via E. Orabona 4, 70125 Bari, Italy

[2] Istituto Nazionale di Geofisica e Vulcanologia, Sezione di Bologna, via D. Creti 12, 40128 Bologna, Italy

[3] IDPA-CNR, via M. Bianco 9, Milan, Italy

[4] British Geological Survey, The Lyell Centre, Edinburgh, United Kingdom

[5] Istituto Nazionale di Geofisica e Vulcanologia, Osservatorio Vesuviano, via Diocleziano 328, 80124, Napoli, Italy

Corresponding author: Daniela Mele (daniela.mele@uniba.it)

Abstract

The knowledge of the Total Grain Size Distribution (TGSD) of the material erupted during explosive volcanic eruptions is one of the main factors for reducing uncertainty in quantitative hazard assessments and forecasts of tephra dispersal. A few TGSDs have been made available in the literature, mostly reconstructed by assuming that tephra deposits consisted of one single component. This simplification can introduce substantial bias in the interpretation of magma fragmentation mechanisms and significantly affect ash dispersion forecasts, since tephra actually include multiple components, such as juveniles, lithics, and crystals, each having a specific aerodynamic behaviour that depends on particle shape, density, and size. To investigate on this problem, in this study we reconstructed TGSDs by considering all components of the eruptive particle mixture. We focussed on the deposits of the Agnano Monte Spina, and Astroni eruptions, as to achieve a more robust quantitative hazard assessment of tephra fallout at Campi Flegrei (Italy). Field investigations and laboratory analyses on samples collected from proximal to distal locations allowed the input data to be obtained for the reconstruction of the TGSDs of juvenile, lithic, and crystal components by means of the Voronoi tessellation method. Results confirm that the bulk TGSD is the combination of the merging of different component subpopulations, each one with its weight. For the first time, this work shows how the systematic reconstruction of the TGSD with the presented method can give important information on magma fragmentation mechanisms, wall-rock erosion processes, and on the

aerodynamic behaviour of each component at variable distances. Finally, the integration of data from distal tephra deposit allowed reassessing the erupted volumes of the eruptions considered in this research.

Keywords: Total grain-size distribution, component analysis, tephra dispersal, magma fragmentation.

1. Introduction

Mechanics of fragmentation of solid rock and viscous fluids has relevance in engineering, geology, geophysics, and industry. This is because it controls particle size and shape and hence influences the transport mechanisms of fragmented particles. In volcanology, the factors controlling the fragmentation mechanisms of magma can be gained only if the total grain size distribution (TGSD) of the erupted material is reliably assessed (Kaminski and Jaupart 1998; Rust and Cashman 2011; Costa et al. 2016). The TGSD reflects the dispersal of the parent grain size distribution in the eruptive plume (Kaminski and Jaupart 1998; Liu et al. 2015, 2017), and allows assessing on tephra particle settling dynamics (Scollo et al. 2008; Costa et al. 2009; Folch 2012; Bonadonna and Costa 2013). Beside and beyond the fragmentation-controlling factors, dispersal and settling behaviour of particles, the TGSD allows better constraining the eruptive budget of a volcano (Sulpizio 2005), the calculation of the energy released at fragmentation (Büttner et al. 2006), and is of paramount importance as input parameter of tephra dispersal simulations and one of the main sources of uncertainty in tephra hazard assessment (e.g., Macedonio et al. 1988; Bonadonna et al. 2015; Costa et al. 2016; Selva et al. 2018). TGSD can be derived from the grain-size distribution of massive pyroclastic density current deposits generated during the collapse of the eruptive column (Macedonio et al. 1988; Folch and Sulpizio 2010) or reconstructed by combining thickness and grain size distribution data of tephra samples collected at multiple locations and integrated using different interpolation techniques (Murrow et al. 1980; Walker 1981; Sparks et al. 1981; Carey and Sigurdsson 1982; Parfitt 1998, Bonadonna and Houghton 2005; Engwell et al. 2015). For TGSDs reconstructed with the latter method, the quality of the results is affected by many factors, such as the number and spatial distribution of sample locations (Bonadonna and Houghton 2005; Bonadonna et al. 2015; Tsunematsu and Bonadonna 2015; Costa et al. 2016). Very few TGSDs are available in the literature and, with the exception of very few cases (e.g. Macedonio et al. 1988; Pfeiffer et al. 2005), generally, they are calculated by assuming that tephra consists of one single effective component (Bonadonna and Houghton 2005; Rose and Durant 2009; Scollo et al. 2014; Tsunematsu and Bonadonna 2015; Costa et al. 2016). However, the grain size distribution of tephra deposits results from the combination of subpopulations of different components (i.e., juvenile, crystal, and lithic fragments), each one characterized by its specific

grainsize distribution. The distributions of the different components of the initial eruptive mixture need to be assessed separately as tephra transportation and sedimentation process are influenced by particle density and shape, which control their terminal velocities (e.g. Palladino et al. 2002; Dellino et al. 2005; Pfeiffer et al. 2005).

In this paper, we reconstructed the TGSDs of juvenile, lithics, and loose crystal components, together with the classical bulk TGSDs of the fallout deposits of Agnano Monte Spina (AMS) and Astroni 6 eruptions at Campi Flegrei (Italy) using the Voronoi tessellation method (Bonadonna and Houghton 2005). We chose these eruptions since they are representative of the large (Agnano Monte Spina) and medium (Astroni 6) events of the Campi Flegrei Caldera (Orsi et al. 2004, 2009; Costa et al. 2009) in the last 5 ka and fallout deposit data up to a distance of 460 km from the vent are available.

We show how the decomposition of bulk TGSD into the TGSD of each component can give insights into the different mechanisms characterizing magma fragmentation and host-rock erosion from conduit walls, also refining the input parameters needed in tephra dispersion simulations.

2. Case Studies

During the last 15 ka, the Campi Flegrei caldera (CFc) has been the site of intense volcanism, with about 70 eruptions (Di Vito et al. 1999; Orsi et al. 2004, 2009; Isaia et al. 2009) grouped into three epochs of activity (15.0-10.6 ka, 9.6-9.1 ka, 5.6-3.8 ka; Di Vito et al. 1999; Isaia et al. 2009; Smith et al. 2011). The eruptions of Agnano-Monte Spina and Astroni 6 well represent the variability in terms of magnitude of the eruptive activity occurred in the third epoch (5.6-3.8 ka, Di Vito et al. 1999; Isaia et al. 2009). For the scope of the present study, we selected the B1 and D1 fallout layers of Agnano Monte Spina (de Vita et al. 1999) and Unit 6 of Astroni (Isaia et al. 2004), for which data from proximal to distal locations, up to 460 km from the vent, were available.

2.1 *Agnano-Monte Spina eruption*

The Agnano-Monte Spina (AMS) eruption (4.5 ka, Smith et al. 2011) was the largest event occurred in the last epoch of CFc activity (5.6-3.8 ka). It was characterized by a magmatic/phreatomagmatic activity (de Vita et al. 1999; Dellino et al. 2001) that led to the emplacement of alternating fall and pyroclastic density current deposits (de Vita et al. 1999; Dellino et al. 2001). The thick sequence of deposits was subdivided into various members and sub-members, named A through E (de Vita et al. 1999).

Two main plinian events generated fallout deposits, named B1 and D1 (de Vita et al. 1999). The B1 fallout deposit was generated during the magmatic phase of the eruption (Dellino et al. 2001), and the column reached a maximum height of about 23 km (de Vita et al. 1999; Costa et al. 2009). The

isopach maps show a north-eastward dispersal of the erupted material (Fig. 1a). The D1 deposit originated from a column that reached a maximum height of about 30 km and was dispersed to the northeast (Fig. 1b) (de Vita et al. 1999; Costa et al. 2009). The deposit volumes of B1 and D1 fallout phases, were estimated (using data collected up to the distance of 45 km from the vent) to be greater than 0.45 and 0.65 km^3, respectively (Dell'Erba 2004). The AMS succession between the B1 and D1 deposits includes both deposits of B2 and C members and an erosional unconformity recovered in several proximal sites. At the distal site of Lago Grande di Monticchio (Wulf et al. 2008) the two tephra layers correlated to the B1 and D1 events (Smith et al. 2011) are separated by continental deposits representative of a pause of tens of years between these tephra layers.

2.2 *Astroni 6 eruption*

The thick stratigraphic succession of Astroni deposits was split into seven units, which represent the products of phreatomagmatic eruptions with subordinate magmatic phases, separated each other by short time intervals (4.3-4.2 ka; Isaia et al. 2004; Smith et al. 2011). The units include mostly pyroclastic density currents, subordinate strombolian deposits, lavas and one subplinian fallout deposit. The latter is part of Unit 6, which was generated during a magmatic phase of the eruption. The fallout deposit originated from an eruptive column of about 14 km (Costa et al. 2009) was mainly dispersed to the east (Fig. 1c; Isaia et al. 2004). For Unit 6, the deposit volume, which includes both the basal fallout and the deposit generated by pyroclastic density currents, was estimated to be greater than 0.23 km^3 (Dell'Erba 2004).

3. Dataset for the reconstruction of the TGSDs of AMS B1, AMS D1 and Astroni 6 phases

The TGSDs of the selected fallout deposits were previously reconstructed by Sandri et al. (2016) and Costa et al. (2016) by means of the Voronoi tessellation method using a limited number of samples (5 for B1 phase, 6 for D1 phase and 4 for Astroni 6; green dots in Fig. 1). The authors used the proximal-medial grain-size data of Pfeiffer and Costa (2004a, b; Fig. 1a, b, c), adding one distal data, which was collected at a distance of about 150 km from the vent (Lake of Monticchio, Sandri et al. 2016) (Fig. 1d). The obtained TGSDs (Costa et al., 2016) show a clear bimodality and a significant fine ash subpopulation. Costa et al. (2016) showed that, in order to obtain a realistic TGSD, it is necessary to integrate grain-size data of sample collected at distances from less than one tenth up to ten-twenty times the column height (up to thirty for strong wind intensity), in order to adequately sample the ash fractions down to 125 μm. This implies that for a column height of about 20-30 km, as in the case of our selected units, the maximum distance of grain size data from the vent should be, at least, about 200-300 km. Thanks to tephrostratigraphic studies carried out over the last 30 years in

137 the Central Mediterranean (Keller et al. 1978; Paterne et al. 1988; Siani et al. 2004; Wulf et al. 2004,
138 2008; Lowe et al. 2007; Sulpizio et al. 2010, 2014; Zanchetta et al. 2011), the presence of distal ash
139 deposits of numerous past eruptions of Italian volcanoes has been recorded. In particular, the distal
140 ash deposits of the Agnano Monte Spina and Astroni eruptions were found up to the distance of 460
141 km from the vent in Lake Shkodra (Sulpizio et al. 2010, 2014). In this work, we used as benchmark
142 the works of Costa et al. (2016) and Sandri et al. (2016), adding three more distal samples for Astroni
143 and four for Agnano Monte Spina located in Adriatic Sea (Siani et al. 2004; Lowe et al. 2007) and
144 Lake Shkodra (Sulpizio et al. 2010; 2014; red dots Fig. 1d). At Lake Shkodra, the Astroni tephra layer
145 was recognized as 1 cm-thick discrete sandy–silty layers (coarse to fine ash) (Sulpizio et al. 2010;
146 2014). We considered as primary tephra only the lower half of the visible layer, while the upper half
147 is considered to be made of reworked sediment. The Agnano Monte Spina tephra is a 5 cm-thick light
148 grey sandy layer (Sulpizio et al. 2010; 2014). The total thickness of Agnano Monte Spina tephra was
149 split into 1 cm attributed to B1 layer and 1.5 cm to D1 layer, and 2.5 cm as reworked. Three samples
150 of Agnano Monte Spina and two samples of Astroni eruptions were recovered in cores from the
151 Adriatic Sea (Siani et al. 2004; Lowe et al. 2007; Fig. 1). We extracted the thickness of 0.5 cm and 1
152 cm for the B1 layer Fig. 1a), and 1 cm and 1.5 cm for the D1 layer of AMS, respectively (Fig. 1b).
153 For Astroni eruption, we extrapolated the thickness of 0.5 cm for both locations (Fig. 1c). Beside the
154 distal data, we added also proximal-medial grain-size data (4 for B1, 2 for D1 and 4 for Astroni) (red
155 dots in Fig. 1).
156 Furthermore, we also used these data in order to recalculate the deposit volumes of the selected fallout
157 units, which were previously determined using only proximal-medial locations (de Vita et al. 1999;
158 Dell'Erba 2004; Isaia et al. 2004; Costa et al. 2009).
159
160 **4. Methods**
161 Both the TGSDs of single components (juvenile, loose crystals, and accessory lithics) and the bulk
162 TGSD, which does not account for the different particle component subpopulations, were
163 reconstructed by using TOTGS code (Biass and Bonadonna 2014), which implements the Voronoi
164 tessellation method (Bonadonna and Houghton 2005). For each location, in order to obtain the grain
165 size distribution and mass load necessary to reconstruct the TGSDs of each component, grain-size,
166 density, and componentry analyses were performed. For the sake of consistency, they were carried
167 out both on the new and old samples.
168 The grain-size analysis of the samples was conducted using mechanical sieving for the size fractions
169 coarser than 3 ϕ (125 μm) at 1 ϕ interval ($\phi = -\log_2(d)$, where d is the particle size in mm). The finer
170 fractions, from 4 ϕ (63 μm) to 9 ϕ (2 μm), were analysed by means of a Beckman Coulter Multisizer

4 (Mele et al. 2015). The median size (Mdϕ) and the sorting parameters (Inman 1952) of each grain-size distribution were calculated using a Fortran 90 code, available into the PYFLOW package (Dioguardi and Dellino 2014).

Density analyses were carried out by using standard Gay-Lussac pycnometers of 5, 10 or 25 ml capacity (depending on the grain-size). For juvenile particles, since their density is a function of grain-size (Houghton and Wilson 1989; Mele and Dioguardi 2018), density was measured on a selected number of particles randomly hand-picked from each grain-size fraction from -4 ϕ to 2 ϕ (i.e. 16 - 0.25 mm range). For the finer fractions, density was estimated by extrapolating the regression curves (Eychenne and Le Pennec 2012) obtained in the measured range (Supp. Fig. 1 shows the variation of density of juvenile material as function of particle size expressed in ϕ units), until it reached the value of the density of dense rock equivalent of fine ash at 6-7 ϕ (16-8 μm). The latter was obtained by density measurements in a pycnometer of crushed juvenile fragments.

Component analysis was carried out on a representative number of particles of each grainsize fraction of the bulk material. For the size fractions in the range from -6 ϕ to 0 ϕ (i.e. 64 - 1 mm), a subsample of particles of each component was hand-picked and weighted; the weight fraction of each component was calculated for each size by scaling the weight of the subsample to the total weight of the sample. For the grainsize range from 1 ϕ to 3 ϕ (i.e. 0.50 – 0.125 mm), particles of each component were counted under a stereomicroscope. The weight of each component was estimated by means of the density of each component in each size fraction.

The mass load of each component at each location was obtained by means of the following equation:

$$Mass\ load = \varphi(\rho_j w_j + \rho_l w_l + \rho_x w_x)T$$

where φ is the porosity of the bulk deposit, ρ and w are the density and volume fraction of component, respectively, and T is the deposit thickness. The subscripts j, l and x refer to juvenile, lithic, and crystal component, respectively. The density of the juvenile component, ρ_j, is the weighted average of the measured density of each size fraction considering its volume fraction. The porosity of the bulk deposit was assumed equal to 40 % at each location, in agreement with the measured deposit density reported by Pfeiffer and Costa (2004a, b).

The isopach maps were reconstructed by extending the proximal-medial ones (Costa et al. 2009), to include the distal thicknesses from Adriatic Sea and Balkans (Fig. 1).

The zero lines, i.e., isolines of zero tephra load, of the three eruptive units, are shown on Fig. 1. They were drawn by extending the shape of the last isopach (Fig. 1a, b and c) to a maximum downwind

distance obtained by extrapolating the regression line in the log(T) vs. Square root of the area (SRA) diagram to a thickness of 0.1 mm (Fig. 2).

The volume of the fallout deposits was calculated by employing two methods: i) combining Pyle (1989) method for proximal deposits (up to 20-30 km) and Sulpizio (2005) method for distal deposits (up to 460 km), and, ii) Bonadonna and Costa (2012) method.

Furthermore, in order to characterize the aerodynamic behaviour of particles, we also calculated the settling velocity of each component constituting the samples collected along the downwind direction (Fig. 3), by means of the drag law of Dioguardi et al. (2017), which is a shape-dependent formula that uses 3D sphericity as shape descriptor. 3D sphericity values of the particles were taken from Mele and Dioguardi (2018) who measured them for the same samples used in this work (Supp. Fig. 2). As the representative particle size, we used the median size (Mdϕ) of the grain size distribution of each component. For simplicity, the density and viscosity of air were assumed to be constant and equal to 0.47 kg m^{-3} and 1.54 10^{-5} Pa s, respectively, which are the height-averaged values over the first 20 km from sea level of the International Standard Atmosphere.

In addition, in order to understand the relationship between TGSD and the vesicle size distribution of the juvenile material, the latter was reconstructed by means of μX-CT imaging carried out with a Bruker Skyscan 1172 high-resolution scanner. Only samples of the D1 phase (pumice size of about 8-16 mm) were scanned, since the vesicle data of B1 and Astroni 6 unit (Fig. 4c) were already available in Mele and Dioguardi (2018). We used the same operating conditions of Mele and Dioguardi (2018) (pixel size of 1.56 μm, X-ray voltage of 70 kV, X-ray current of 141 μA, Rotation step of 0.2 degree; Filer = Al 0.5 mm). The 3D vesicle size distribution was obtained selecting a volume of interest (VOI) of 16 mm^3 and using a sphere-fitting algorithm, which is based on two steps, i.e. a "skeletonisation" to identify the medial axis of all structures, and a "sphere-fitting" to measure the local thickness of all voxels lying along this axis (Remy and Thiel 2002).

5. Results

As first result, the integration of distal ash data allowed the re-calculation of the volume of fallout deposits (Table 1), which were found to be greater than those estimated on the basis of proximal-medial locations only (de Vita et al. 1999; Dell'Erba 2004; Isaia et al. 2004; Costa et al. 2009). The three fallout deposits (Fig. 2) exhibit multiple segments on log(*T*) vs. SRA diagrams (e.g. Fierstein and Nathenson 1992; Bonadonna and Houghton 2005). The slope of the segments is steeper at proximal locations up to about 40 km and 27 km for Agnano Monte Spina and Astroni 6 eruptions, respectively (Fig. 2), and it becomes gentler for larger distances, which is a typical feature of plinan and subplinan fallout deposits (Rose 1993; Sparks et al. 1992; Sulpizio 2005; Bonadonna and Costa

2012). The estimated tephra volumes for B1, D1 and Astroni 6 using Pyle (1989) and Sulpizio (2005) methods, are 1.56, 1.62, and 0.63 km^3, while using Bonadonna and Costa (2012), are 1.23, 2.04, and 0.42 km^3.

The three components of all deposits show a similar trend of median grainsize (Fig. 3a) and weight fraction (Fig. 3b) at increasing distance from the vent. By inspecting the data of samples collected along the downwind direction, it is shown that the median size (Mdϕ), expressed in ϕ units, of the juvenile and lithic components increases at increasing distance from the vent (meaning that fragment size in mm decreases). On the other hand, the median size of crystals (in ϕ units) does not show a significant variation at increasing the distance from the vent (Fig. 3a). The content of the juvenile component first decreases from proximal to intermediate distance from the vent, then increases to become the main component in the distal locations, i.e. starting from a distance of about 120 km from the vent (Fig. 3b). The content of loose crystals and accessory lithics shows an opposite trend as compared to juvenile particles (Fig. 3b). The content of lithics and loose crystals is negligible in distal samples (beyond 150 km), which are almost entirely made of juvenile fragments.

Figure 3c shows plots of terminal velocities of each component at different locations and for each eruptive unit. The settling velocities of crystal particles do not show any significant variation at increasing distance from the vent. Juvenile and lithic particles, instead, show similar decreasing trends of settling velocities with increasing distance. This behaviour indicates that there is grain size selectivity of the two components and that they can be considered as hydraulically equivalent (Fig. 3c).

TGSD of both single components and bulk tephra is shown in Figure 4. In order to identify the presence of different subpopulations inside of the TGSDs, i.e. coarse and fine subpopulations, a bi-Gaussian distribution was employed (Fig. 4 and Supp. Fig. 3; Table 2), following the approach proposed by Costa et al. (2016). The TGSDs of the single components show that the bulk bimodal TGSDs result from the combination of different subpopulations of particles, each characteristic of a specific component. For all deposits, the finer subpopulation (mode at 6 ϕ) represents the largest portion of the total distribution, and it is composed of juvenile particles. The latter also shows a coarser subpopulation, which is a small percentage of the coarse subpopulation of the bulk TGSD (Fig. 4). The mode of the coarser juvenile subpopulation is -3 ϕ for B1 unit and Astroni 6 and -4 ϕ for D1.

The TGSDs of lithic and crystal components are unimodal and well discriminated from those of the juvenile particles (Fig. 4 and Supp. Fig. 3). The mode of lithic population is 0 ϕ for B1 and -1 ϕ for D1 and Astroni 6. The mode of crystal population is ~1 ϕ for all the deposits.

By means of the TGSD of single components, it was also possible to estimate the fraction of the components for each eruptive unit. The percentage of juvenile particles is always larger than that of the other components with 76 % for Astroni 6, and 63 % and 62 % for B1 and D1 of Agnano Monte Spina eruptions, respectively (Fig. 4). The volume of lithics, juvenile and crystals of each eruptive unit was also estimated by combining the single abundances with the tephra volume (Table 1).
In addition, for comparison with TGSDs, also bubble distribution characterizing pumices as function of ϕ (Mele and Dioguardi 2018) were analysed and are reported in Figure 4.

6. Discussion and conclusion

TGSDs of the different components of fallout deposits are here reported for the first time. Before to discuss in depth the significance of the TGSD, it is important to consider the main sources of uncertainty as: i) the definition of the zero-mass isoline, which is needed as a constraint of outermost polygons area; and, ii) the number of analysed samples and their spatial distribution. In the present work, the first issue was accounted by drawing the zero line as the extrapolation of the distal regression line in the Log(T) vs. SRA diagrams (Fig. 2). The second issue was accounted by integrating the original dataset of Costa et al. (2016) and Sandri et al. (2016) with new grainsize analyses, especially from distal locations (up to 460 km from the vent). The implementation of data yielded, as first result, a new calculation of volumes, which are greater than about 240 %, 150% and 174% the previous estimations for B1, D1 and Astroni 6, respectively. The addition of distal data also led to a significant change of the bulk TGSD presented in the former papers, with a shift of the mode of the fine subpopulation from 3 to 6 ϕ (B1 and D1 unit) and 4 to 6 ϕ (Astroni 6 unit). It is worth noting that our TGSDs were derived from data collected at distances from the vent that are not influenced from the pyroclastic deposition of the column margins (Fig. 1), as also confirmed by the absence of ballistic blocks inside the deposits. This may result in some underestimation of coarse populations, which, in any case, represent only a minor fraction with respect to the whole grain size distribution.
The analysis of the componentry of TGSDs of fallout deposits, combined with the bubble size distributions of pumices (Fig. 4), shed light into magma fragmentation mechanisms. The bulk TGSD was, in fact, reconstructed as the combination of the grainsize distributions of different component subpopulations (juvenile, lithic, and crystal particles; Fig. 4), demonstrating that the proportion of fine and coarse subpopulations in the bulk TGSDs (Fig. 4) depends on the weight of each component. In particular, the weight of the coarse subpopulation of the bulk TGSD results from the overlap of juvenile, lithic, and crystal populations (Fig. 4). For B1 and D1, which have a higher content of lithic

and crystal fragments than Astroni 6, the coarse subpopulation is represented for 81% and 92% by the densest component and for 19% and 8% by juvenile particles, respectively. For Astroni 6, the coarse population is made up by 50% of juvenile component and 50% of lithic and crystal particles.

The TGSDs of crystals (that can be described as Gaussian distribution in ϕ units) likely represents the original size distribution of phenocrysts, which were released at magma fragmentation. For all three eruptions, the crystal TGSDs are very similar and are well described by a lognormal function with the mode ranging from 0.23 ϕ for AMS D1 to 0.5 ϕ for Astroni 6 and standard deviation of about 0.8-1.1 ϕ (see Table 2).

Also lithics, which are generated by the erosion of country rocks of the volcanic conduit due to fragmentation and thermo-mechanical abrasion from the pyroclastic mixture (Campbell et al. 2013; Massaro et al. 2018), show lognormal TGSDs, and their average size can be related to mechanical properties of wall rocks and erosion energy (Macedonio et al. 1994; Costa et al. 2009b). The lithic volume increases as eruption intensity increases, from Astroni 6 (16%) to AMS B1 (23%) and AMS D1 (25%) eruptions (Table 1).

The TGSD of the juvenile component, likely being a result of magma fragmentation, is more complex to interpret, as it shows a marked bimodality. Complexities in juvenile grain-size distributions can be related to inhomogeneity of vesicle sizes in the magma. The coarse subpopulations show a mode of about -3 ϕ and a standard deviation of ~1.0-1.4 ϕ for all the three eruptions and has a significantly lower weight with respect to the finer one (see Table 2). It represents the coarse fragmentation of rising magma, and yields information on magma vesicularity. The fine-grained subpopulations are the dominant ones and have a mode of about 5 ϕ and a standard deviation of ~1.3-1.5 ϕ for all the three eruptions (see Table 2). The fine-grained subpopulation can be related either to secondary fragmentation of coarser fragments within the volcanic conduit (Costa et al., 2016; Jones and Russel, 2017) or to an intensive brittle fragmentation of a fragile highly-vesicular magma (Zimanowski et al. 2003; Büttner et al. 2006; Dellino et al. 2012). In both cases the mechanical strength of juvenile material is influenced by the abundance and vesicles (Heap et al. 2014) and smaller bubbles can act as local amplificatory of the stress distribution within the material, controlling fragmentation. As shown in Figure 4, the weight % of the size-distribution of particles smaller than 0 ϕ of the TGSDs of the three eruptions presents a significant correlation with the bubble size distribution (correlation coefficient between BSD(ϕ) and TGSD (ϕ+1) is equals to 0.76, 0.63, and 0.88 for B1, D1, and Astroni 6, respectively). The correlation can be interpreted as the fine vesicle population controls the grain-size distribution of the fine-grained population of the juvenile material, with vesicles representing the preferred weakness location of the fragmenting material. Indeed, when the fragmentation processes intercept a vesicle, it produces particles finer than the vesicle itself. For example, the fragmentation

of bubbles of 1 ϕ dimension will produce fragments finer than 1 ϕ and the same time the other vesicles will produce fragments finer than their dimensions. This processes, combined with vesicle abundance, explains the grain size distribution of fine juvenile grain population. Therefore, as suggested by Liu et al. (2017), Mele and Dioguardi (2018), the size of fine ash particles may result from the size and spatial distribution of the pre-fragmentation bubble population.

The integration of component analysis, TGSD and settling velocity data helps to characterize both the aerodynamic behaviour of each component and their parent grain size, allowing also explaining the behaviour of each component at increasing distance from the vent. The juvenile and lithic components show the same settling velocity decay law at increasing distance from the vent (Fig. 3a). They settle with similar terminal velocities (Fig. 3c), and hence the two components are hydraulically equivalent. The progressive increase of lithic content, up to a maximum value at medial locations (Fig. 3b), can be related to the lithic size in the deposit approaching the mode of the parent grain-size distribution, i.e. lithic TGSD (Fig. 4 and Supp. Fig. 3). The content of juvenile fragments follows an opposite trend from proximal to medial locations (Fig. 3b) but at distal locations, they become the main component. This behaviour can be related to its parent grain-size distribution, which is characterized by a large part of finer particles (Fig. 4 and Supp. Fig. 3) that travel for long distances from the vent. On the other hand, the crystal particles have the same settling velocity at all locations, meaning that their transportation mechanism is not selective in terms of grain size but reflects the fact that the parent crystal TGSD (Fig. 4 and Supp. Fig. 3) has a relatively very narrow grain-size distribution already at fragmentation. This would also explain the increase of crystals up to medial locations where the maximum probability of sedimentation, given by the average size of their TGSD, is reached.

Finally, it is worth noting that knowing the contribution of each component to the TGSD helps refining the input parameters needed in tephra dispersion simulations (e.g. Costa et al. 2016) and tephra hazard assessment (e.g. Selva et al. 2018). As it has been shown in this work, the different components can have completely different aerodynamic behaviours as resulting from their specific grainsize, density distribution, and shape. The usual assumption of a single-component tephra made when performing tephra dispersion simulation can then be overcome by means of multi-component TGSDs with the aim at improving dispersion modelling.

Acknowledgments

This work has benefited from funding provided by the Italian Presidenza del Consiglio dei Ministri - Dipartimento della Protezione Civile (DPC), agreement INGV-DPC 2015-2016. This paper does not

necessarily represent the DPC official opinion and policies. A.C., G.M., and R.I. acknowledge the European project EUROVOLC (grant agreement number 731070) and the MIUR project Premiale Ash-RESILIENCE. Published with permission of the Executive Director of British Geological Survey (UKRI).

References

Biass S., Bonadonna C (2014) TOTGS: Total grainsize distribution of tephra fallout. https://vhub.org/resources/3297

Bonadonna C, Houghton BF (2005) Total grain-size distribution and volume of tephra-fall deposits. Bull Volcanol 67: 441–456

Bonadonna C, Costa A (2012) Estimating the volume of tephra deposits: A new simple strategy. Geology 40(5):415-418

Bonadonna C, Costa A (2013) Plume height, volume, and classification of explosive volcanic eruptions based on the Weibull function. Bull Volcanol 75(8):742

Bonadonna C, Biass S, Costa A (2015) Physical characterization of explosive volcanic eruptions based on tephra deposits: Propagation of uncertainties and sensitivity analysis. J Volcanol Geotherm. Res 296:80-100

Büttner R, Dellino P, Raue H, Sonder I, Zimanowski B (2006) Stress induced brittle fragmentation of magmatic melts: Theory and Experiments. J Geophys Res 111:B08204

Campbell ME, Russell J, Porrit LA (2013) Thermomechanical milling of accessory lithics in volcanic conduits. Earth Planet Sci Lett 377-378:276-286

Carey SN, Sigurdsson H (1982) Influence of particle aggregation on deposition of distal tephra from the May 18, 1980, eruption of Mount St. Helens volcano. J Geophys Res 87(B8):7061–7072

Costa A, Dell'Erba F, Di Vito M, Isaia R, Macedonio G, Orsi G, Pfeiffer T (2009) Tephra fallout hazard assessment at the Campi Flegrei caldera (Italy). Bull Volcanol 71:259–273

Costa A, Sparks RSJ, Macedonio G, Melnik O (2009b) Effects of wall-rock elasticity on magma flow in dykes during explosive eruptions. Earth Planet Sci Lett 288: 455-462

Costa A, Pioli L, Bonadonna C (2016) Assessing tephra total grain-size distribution: Insights from field data analysis. Earth Planet Sci Lett 443:90–107

de Vita S, Orsi G, Civetta L, Carandente A, D'Antonio M, Di Cesare T, Di Vito MA, Fisher RV, Isaia R, Marotta E, Ort M, Pappalardo L, Southon J (1999) The Agnano-Monte Spina eruption in the densely populated, restless Campi Flegrei caldera (Italy). J Volcanol Geotherm Res 91:269–301

Di Vito MA, Isaia R, Orsi G, Southon J, de Vita S, D'Antonio M, Pappalardo L, Piochi M (1999) Volcanic and deformational history of the Campi Flegrei caldera in the past 12 ka. J Volcanol Geotherm Res 91:221–246

Dell'Erba F (2004) Definizione di parametric fisici di alcune eruzioni esplosive della caldera dei Campi Flegrei negli ultimi 15 ka: implicazioni per la valutazione della pericolosità vulcanica. Ph.D. thesis, Bari, University of Bari, 147 pp.

Dellino P, Isaia R, La Volpe L, Orsi G (2001) Statistical analysis of textural data from complex pyroclastic sequences: implication for fragmentation processes of the Agnano-Monte Spina Tephra (4.1 ka), Phlegraean Fields southern Italy. Bull Volcanol 63:443–461

Dellino P, Mele D, Bonasia R, Braia G, La Volpe L, Sulpizio R (2005). The analysis of the influence of pumice shape on its terminal velocity. Geophys Res Lett 32, L21306

Dellino P, Gudmundsson MT, Larsen G, Mele D, Stevenson J A, Thordarson T, Zimanowski B (2012) Ash from the Eyjafjallajökull eruption (Iceland): fragmentation processes and aerodynamic behaviour. J Geophys Res 117:B00C04. https://doi.org/10.1029/2011JB008726.

Dioguardi F, Dellino P (2014) PYFLOW: a computer code for the calculation of the impact parameters of Dilute Pyroclastic Density Current (DPDC) based on field data. Comput Geosci 66: 200–210

Dioguardi F, Mele D, Dellino P, Dürig T (2017) The terminal velocity of volcanic particles with shape obtained from 3D X-ray microtomography. J Volcanol Geotherm Res 329:41–53

Eychenne J, Le Pennec J (2012) Sigmoidal particle density distribution in a subplinian scoria fall deposit. Bull Volcanol 74:2234-2249

Engwell SL, Aspinall WP, Sparks RSJ (2015) An objective method for the production of isopach maps and impications for the estimation of tephra deposit. Bull Volcanol 77:61

Fierstein J, Nathenson M (1992) Another look at the calculation of tephra fallout volumes. Bull Volcanol 54:156–167

Folch A, Sulpizio R (2010) Evaluating long-range volcanic ash hazard using supercomputing facilities: Application to Somma-Vesuvius (Italy), and consequences for civil aviation over the Central Mediterranean Area. Bull Volcanol 72:1039–1059

Folch A (2012) A review of tephra transport and dispersal models: evolution, current status, and future perspectives. J Volcanol Geotherm Res 235–236(1):96–115

Heap MJ, Xu T, Chen C (2014) The influence of porosity and vesicle size on the brittle strength of volcanic rocks and magma. Bull Volcanol 76:856

Houghton BF, Wilson CJN (1998) Fire and water: the physical roles of water in caldera eruptions at Taupo and Okataina volcanic centres. Water–Rock Interaction, Taupo, New Zealand, pp 25–30.

Inman DL (1952) Measures of describing the size distribution of sediments. J Sediment Petrol 22:125–145

Isaia R, D'Antonio M, Dell'Erba F, Di Vito M, Orsi G (2004) The Astroni volcano: the only example of close eruptionswithin the same vent area in the recent history of the Campi Flegrei caldera (Italy). J Volcanol Geotherm Res 133:171–192

Isaia R, Marianelli P, Sbrana A (2009) Caldera unrest prior to intense volcanism in Campi Flegrei (Italy) at 4.0 ka B.P.: implications for caldera dynamics and future eruptive scenarios. Geophys Res Lett 36:L21303. http://dx.doi.org/10.1029/2009GL040513

Jones TJ, Russel JK (2017) Ash production by attrition in volcanic conduits and plumes. Scientific Report 7:5538. http://dx.doi.org/10.1038/s41598-017-05450-6

Kaminski E, Jaupart C (1998) The size distribution of pyroclasts and the frag-mentation sequence in explosive volcanic eruptions. J Geophys Res 103: 29759–29779

Keller J, Ryan WBF, Ninkovich D, Altherr R (1978) Explosive volcanic activity in the Mediterranean over the past 200,000 years as recorded in deep-sea sediments. Geol Soc Am Bull 89:591-604

Liu E J, Cashman KV, Rust AC, Gislason SR (2015) The role of bubbles in generating fine ash during hydromagmatic eruptions. Geology 43(3):239-242

Liu E J, Cashman KV, Rust AC, Höskuldsson A (2017) Contrasting mechanisms of magma fragmentation during coeval magmatic and hydromagmatic activity: the Hverfjall Fires fissure eruption Iceland. Bull Volcanol 79:68

Lowe JJ, Blockley S, Trincardi F, Asioli A, Cattaneo A, Matthews IP, Pollard M, Wulf S (2007) Age modelling of late Quaternary marine sequences in the Adriatic: towards improved precision and accuracy using volcanic event stratigraphy. Cont Shelf Res 27:560–582

Macedonio G, Pareschi MT, Santacroce R (1988) A numerical simulation of the Plinian fall phase of 79 A.D. eruption of Vesuvius. J Geophys Res 93:14817-14827

Macedonio G, Dobran F, Neri A (1994) Erosion processes in volcanic conduits and an application to the AD 79 eruption of Vesuvius. Earth Planet Sci Lett 121:137-152

Massaro S, Costa A, Sulpizio R (2018) Evolution of the magma feeding system during a Plinian eruption: The case of Pomici di Avellino eruption of Somma-Vesuvius, Italy. Earth Planet Sci Letter 482:545-555

Mele D, Dioguardi F, Dellino P, Isaia R, Sulpizio R, Braia G (2015) Hazard of pyroclastic density currents at the Campi Flegrei Caldera (Southern Italy) as deduced from the combined use of face architecture, physical modeling and statistics of the impact parameters. J Volcanol Geotherm Res 299:35-53

Mele D, Dioguardi F (2018) The grain size dependency of vesicular particle shapes strongly affects the drag of particles. First results from microtomography investigations of Campi Flegrei fallout deposits. J Volcanol Geotherm Res 353(15):18–24

Murrow PJ, Rose WI, Self S (1980) Determination of the total grain size distribution in a Vulcanian eruption column, and its implications to stratospheric aerosol perturbation. Geophys Res Lett 7:893–896

Orsi G, Di Vito MA, Isaia R (2004) Volcanic hazard assessment at the restless Campi Flegrei caldera. Bull Volcanol 66:514–530

Orsi G, Di Vito MA, Selva J, Marzocchi W (2009) Long-term forecasting of eruption style and size

523 at Campi Flegrei caldera (Italy). Earth Planet Sci Lett 287:265–276
524
525 Palladino DM, Simei S (2002) Three types of pyroclastic currents and their deposits: examples from
526 the Vulsini Volcanoes, Italy. J Volcanol Geotherm Res 116:97–118
527
528 Parfitt E (1998) A study of clast size distribution, ash deposition and fragmentation in a Hawaiian-
529 style volcanic eruption. J Volcanol Geotherm Res 84:197–208
530
531 Paterne M, Guichard F, Labeyrie J (1988) Explosive activity of the south Italian volcanoes during the
532 past 80,000 years as determined by marine tephrochronology. J Volcanol Geotherm Res 34:153–172
533
534 Pfeiffer T, Costa A (2004a) A numerical reconstruction of fall deposits from Agnano-Monte Spina
535 (4100 BP) Plinian eruption in the Campi Flegrei area, Italy, Osservatorio Vesuviano-INGV, Naples,
536 Italy. Report (1), Prot. N. 4440 (10.9.2004). http://www.earth-prints.org/handle/2122/2068
537
538 Pfeiffer T, Costa A (2004b) Reconstruction and analysis of a sub-Plinian fall deposits from the
539 Astroni volcano (ca. 4100–3800 BP) in the Campi Flegrei area, Italy, Osservatorio Vesuviano-INGV,
540 Naples, Italy. Report (2), Prot. N. 4440 (10.9.2004). http://www.earth-prints.org/handle/2122/2069
541
542 Pfeiffer T, Costa A, Macedonio G (2005) A model for the numerical simulation of tephra fall deposits.
543 J Volcanol Geotherm Res 140:273-294
544
545 Pyle DM (1989) The thickness, volume and grain size of tephra fall deposits. Bull Volcanol 51:1–15
546
547 Remy E, Thiel E (2002) Medial axis for chamfer distances: computing look-up tables and
548 neighbourhoods in 2D or 3D. Pattern Recogn. Lett. 23 (6):649–661
549
550 Rose WI (1993) Comment on "another look at the calculation of tephra fallout volumes" by Judy
551 Fierstein and Manuel Nathenson. Bull Volcanol 55:372–374
552
553 Rose W, Durant A (2009) Fine ash content of explosive eruptions. J Volcanol Geotherm Res
554 186:32–39
555
556 Rust AC, Cashman KV (2011) Permeability controls on expansion and size distributions of
557 pyroclasts. J Geophys Res 116 (B11)
558
559 Sandri L, Costa A, Selva J, Tonini R, Macedonio G, Folch A, Sulpizio R (2016) Beyond eruptive
560 scenarios: assessing tephra fallout hazard from Neapolitan volcanoes. Scientific Reports 6:24271
561
562 Scollo S, Folch A, Costa A (2008) A parametric and comparative study of different tephra fallout
563 models. J. Volcanol Geotherm Res 176:199-211
564
565 Scollo S, Prestifilippo M, Pecora E, Corradini S, Merucci L, Spata G, Coltelli M (2014). Eruption
566 column height estimation of the 2011-2013 Etna lava fountains. Annals Geophys 57
567
568 Selva J, Costa A, De Natale G, Di Vito MA, Isaia R, Macedonio G (2018) Sensivity test and esemble
569 hazard assessment for tephra fallout at Campi Flegrey, Italy. J Volcanol Geotherm Res 351:1–28
570
571 Siani G, Sulpizio R, Paterne M, Sbrana A (2004) Tephrostratigraphy study for the last 18,000 ^{14}C
572 years in a deep-sea sediment sequence for the South Adriatic. Quat Sci Rev 23:2485–2500
573

574 Smith VC, Isaia R, Pearce NJG (2011) Tephrostratigraphy and glass compositions of post-15 kyr
575 Campi Flegrei eruptions: implications for eruption history and chronostratigraphic markers. Quat Sci
576 Rev 30:3638–3660
577
578 Sparks RSJ, Wilson L, Sigurdsson H (1981) The pyroclastic deposits of the 1875 eruption of Askja,
579 Iceland. Philos Trans R Soc Lond, A 229:241–273
580
581 Sparks RSJ, Bursik MI, Ablay GJ, Thomas RME, Carey SN (1992) Sedimentation of tephra by
582 volcanic plumes. 2: Controls on thickness and grain-size variations of tephra fall deposits. Bull
583 Volcanol 54:685–695
584
585 Sulpizio R (2005) Three empirical methods for the calculation of distal volume of tephra-fall deposits.
586 J Volcanol Geotherm Res 145:315–336
587
588 Sulpizio R, Van Wleden A, Caron B, Zanchetta G (2010) The Holocene tephrostratigraphic records
589 of Lake Shkodra (Albania and Montenegro). J Quat Scie 25(5):633–650
590
591 Sulpizio R, Zanchetta G, Caron B, Dellino P, Mele D, Giaccio B, Insinga D, Paterne M, Siani G,
592 Costa A, Macedonio G, Santacroce R (2014) Volcanic ash hazard in the Central Mediterranean
593 assessed from geological data. Bull Volcanol 76:866
594
595 Tsunematsu K, Bonadonna C (2015) Grain-size features of two large erup-tions from Cotopaxi
596 volcano (Ecuador) and implications for the calculation of the total grain-size distribution. Bull
597 Volcanol 77 (7):64
598
599 Walker GPL (1981) Plinian eruptions and their products. Bull Volcanol 44:223–240
600
601 Wulf S, Kraml M, Brauer A, Keller J, Negendank JFW (2004) Tephrochronology of the 100 ka
602 lacustrine sediment record of Lago Grande di Monticchio (southern Italy). Quat Int 122:7–30
603
604 Wulf S, Kraml M, Keller J (2008) Toward a detailed distal tephrostratigraphy in the Central
605 Mediterranean: The last 20,000 yrs record of Lago Grande di Monticchio. J Volcanol Geotherm Res
606 177:118-132
607
608 Zanchetta G, Sulpizio R, Roberts N, Cioni R, Eastwood WJ, Siani G, Caron B, PaterneM, Santacroce
609 R (2011) Tephrostratigraphy, chronology and climatic events of the Mediterranean basin during the
610 Holocene: an overview. The Holocene 21:33–52
611
612 Zimanowski B, Wohletz K, Dellino P, Büttner R (2003) The volcanic ash problem. J Volcanol
613 Geotherm Res 122:1–5
614
615
616

617 *Figure Captions*

618 Figure 1. Isopach maps (modified after Costa et al. 2009) of **a** B1 fallout deposit of Agnano Monte
619 Spina eruption, **b** D1 fallout deposit of Agnano Monte Spina eruption, **c** fallout deposit of Astroni 6
620 eruption. **d** Position of the zero-mass isoline (i.e. zero line) used for the compilation of the TGSDs
621 with the Voronoi tessellation technique. The green dots mark the locations of samples used in Costa

et al. (2016); the red dots mark the locations of new samples collected in this work. The black triangles represent the vent of selected eruptions.

Figure 2. a) Semilog plots of thickness versus square root of isopach area, used to calculate the volume of tephra volume combining Pyle (1989) and Sulpizio (2005) methods; b) Semilog plots of thickness versus square root of isopach area showing the Weibull best fit (Bonadonna and Costa, 2013) for tephra deposits of B1 and D1 phase of Agnano Monte Spina eruption (B1-AMS and D1-AMS), and Astroni 6 eruption. θ is a thickness scale; λ is the characteristic decay length scale of deposit thinning; n is the shape parameter (Bonadonna and Costa, 2013).

Figure 3. Comparison of **a** median grain size (Mdϕ) of bulk deposit and juvenile lithic and crystal component along downwind axis, **b** weight percent of juvenile, lithic and crystal component along downwind axis, **c** settling velocity of juvenile, lithic and crystal component along downwind axis.

Figure 4. **a** TGSD (grey rectangles) of bulk deposit of B1 and D1 phase of Agnano Monte Spina eruption (B1-AMS and D1-AMS), and Astroni 6 eruption. Dotted lines show the coarse and fine sub-populations whose sum (full line) fit the observed distribution. **b** TGSD of juvenile, lithic and crystal components, with their weight percentage. **c** Vesicle size distribution histograms;

Supplementary material

Supplementary material Figure 1. Size vs. density diagrams of juvenile component. The vertical dashed line shows the density value of dense rock equivalent.

Supplementary material Figure 2. TGSD of juvenile, lithic, and crystal components. Lines show the coarse and fine sub-populations whose sum (full line) fit the observed distribution.

Supplementary material Figure 2. 3D sphericity vs. size diagram of pumices of B1 phase of Agnano Monte Spina, and Astroni 6 eruptions (after Mele and Dioguardi 2018). 3D sphericity of pumices of D1 phase (Agnano Monte Spina eruption) was assumed equal to particles of B1 phase. Error bars for each grainsize are shown. The solid black line represents the best fit, of which correlation equations and coefficients are displayed.

Figure 1

Click here to download Figure Fig.01.jpg

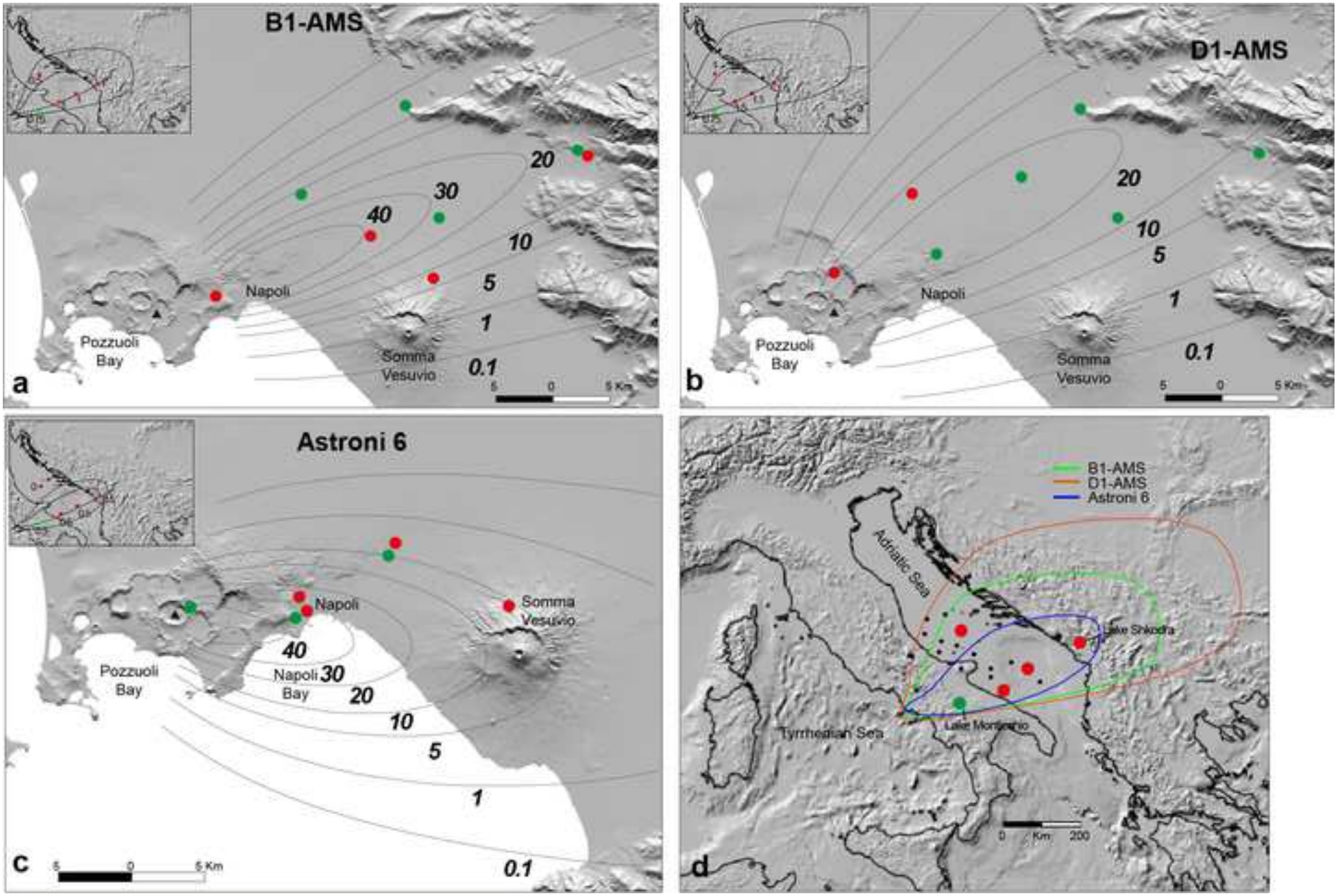

Figure 2

Click here to download Figure Fig.02.jpg

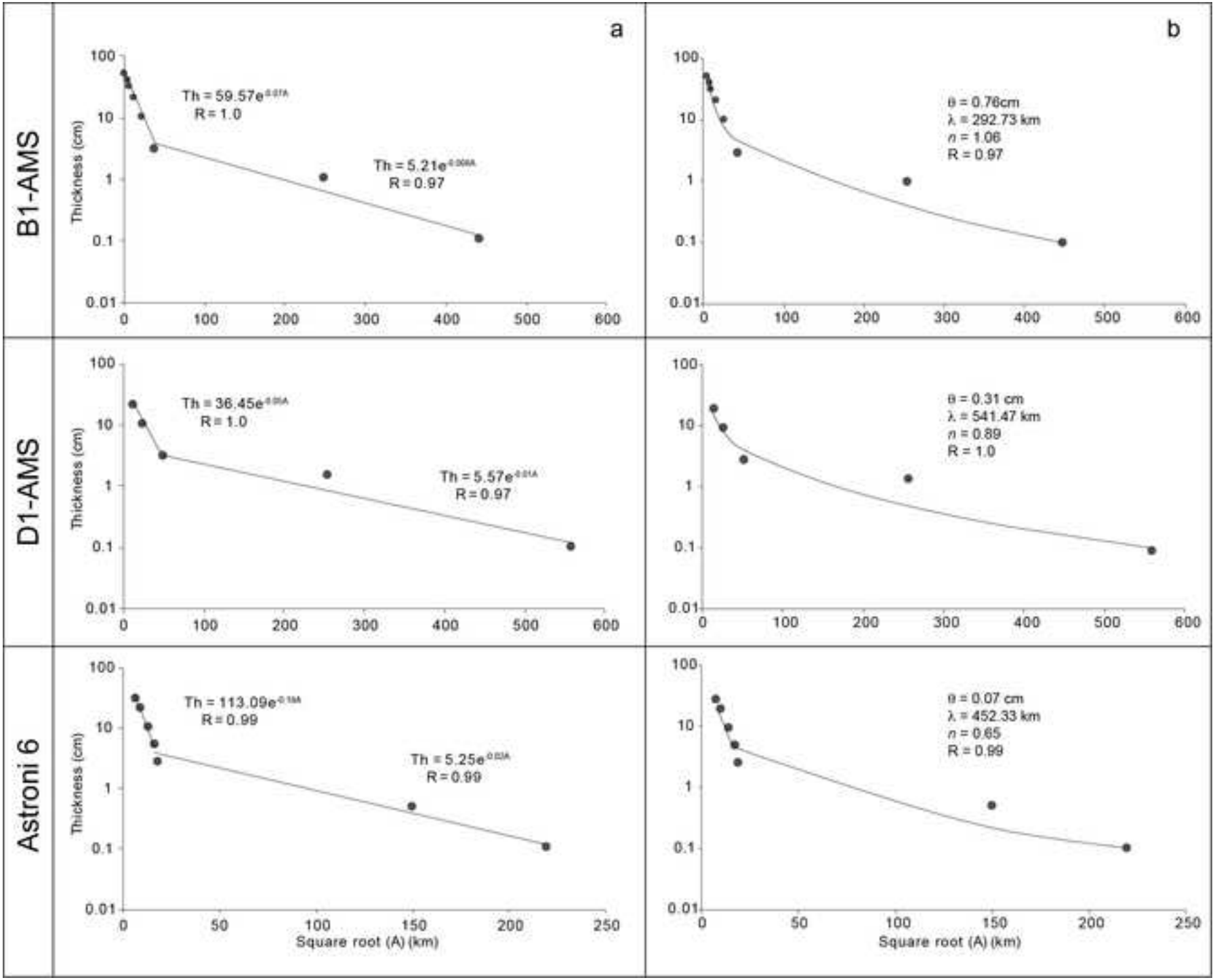

Figure 3

Click here to download Figure Fig.03.jpg

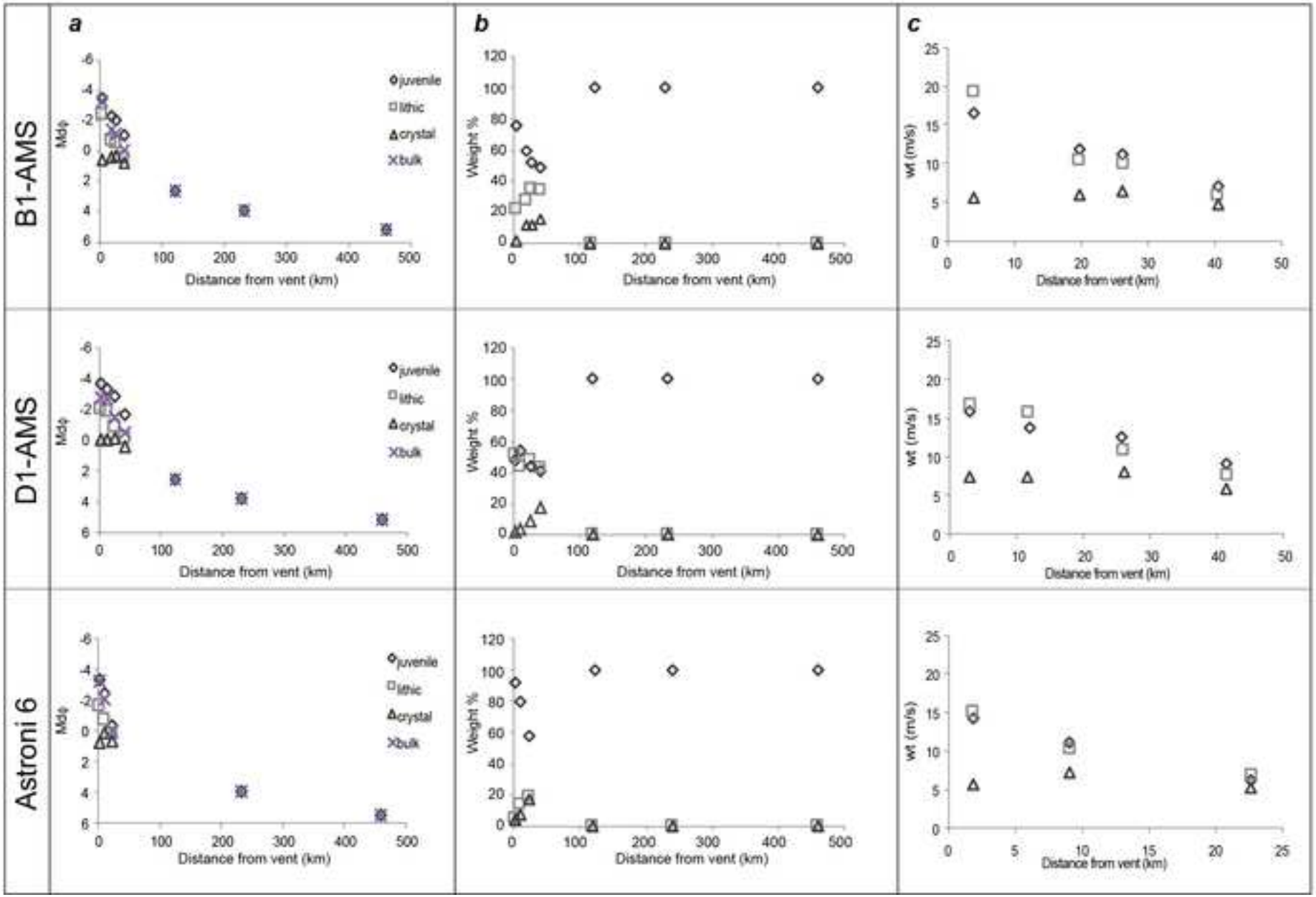

Figure 4

Click here to download Figure Fig.04.jpg

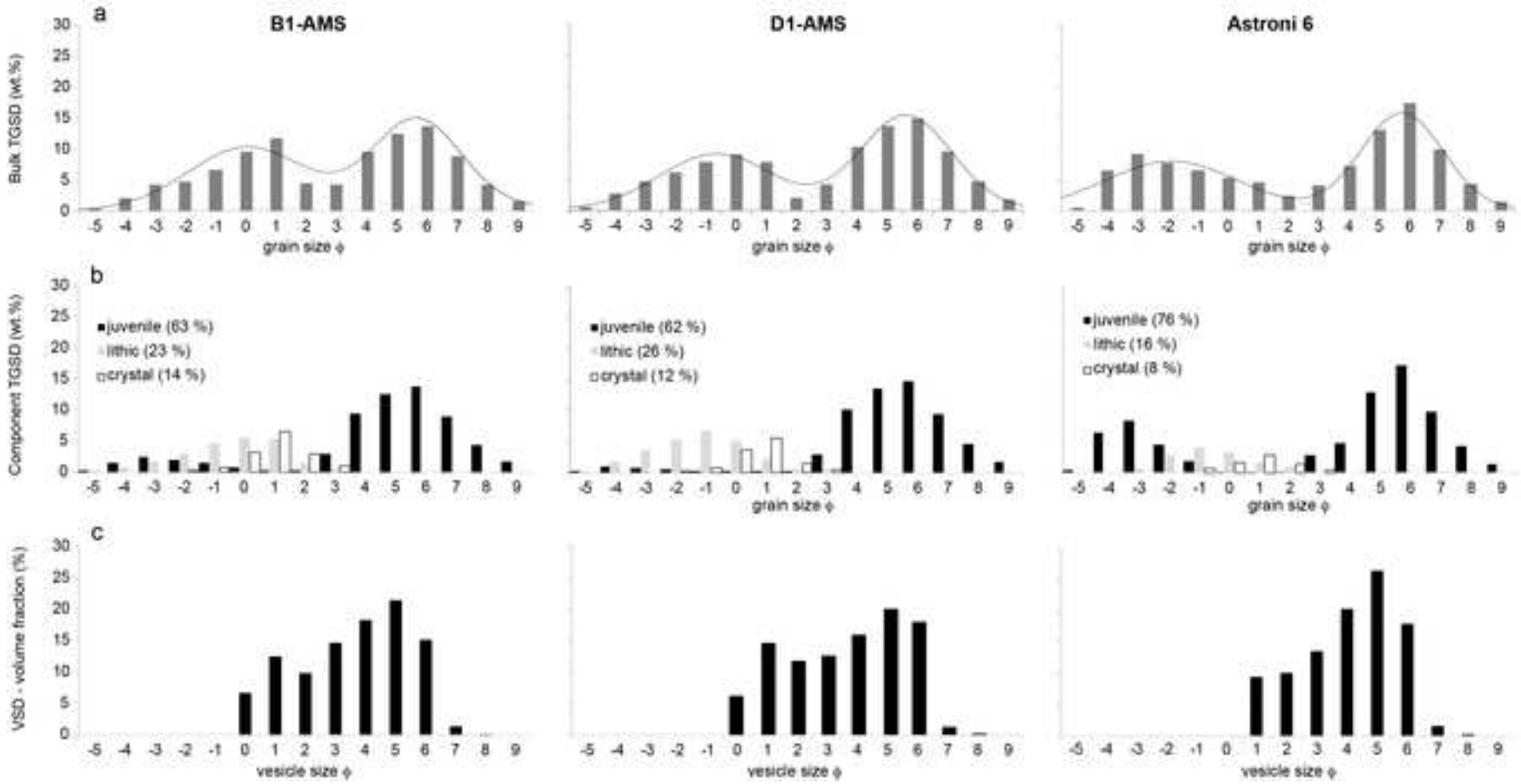

Table 1

	H_t (km)	V_{prox} (km^3)	V_{dist} (km^3)	$V_{t\ juv}$ (km^3)	$V_{t\ lith}$ (km^3)	$V_{t\ xx}$ (km^3)	V_t (km^3)	V_t* (km3)	V_t** (km^3)
Astroni 6	14	0.08	0.55	0.48	0.10	0.05	0.63	0.42	0.23
B1-AMS	23	0.22	1.33	0.97	0.36	0.22	1.55	1.23	0.45
D1-AMS	30	0.24	1.38	0.99	0.43	0.20	1.62	2.04	0.65

Table 1 – Physical parameters of the column phases B1 and D1 units of Agnano Monte Spina and Astroni 6 eruptions. H_t = maximum column height (de Vita et al., 1999; Isaia et al., 2004; Costa et al., 2009). V_{prox}, V_{dist}, V_t, $V_{t\ juv}$, $V_{t\ lith}$ and $V_{t\ xx}$ are the proximal volume, the minimum distal volume, the total volume, the juvenile volume, the lithic volume and crystal volume, respectively, calculated combining Pyle (1989) and Sulpizio (2005) methods. V_t* is the tephra volume calculated using Bonadonna and Costa (2012) method. V_t** is the tephra volume calculated by Dell'Erba (2004) using only proximal-medial locations.

Table 2

Bi-Gaussian parameters	Astroni U6 (Bulk)	AMS B1 (Bulk)	AMS D1 (Bulk)	Astr. U6 (juv)	AMS B1 (juv)	AMS D1 (juv)	Astr. U6 (lith)	AMS B1 (lith)	AMS D1 (lith)	Astr. U6 (crys)	AMS B1 (crys)	AMS D1 (crys)
p	0.44	0.26	0.42	0.29	0.13	0.05	1	1	1	1	1	1
$\mu_1 (in\ \phi)$	-2.37	-1.30	-1.16	-3.59	-3.04	-3.70	-1.23	-0.67	-1.73	0.50	0.47	0.23
$\sigma_1 (in\ \phi)$	2.19	1.84	1.89	1.02	1.39	1.21	1.47	1.61	1.58	1.15	0.92	0.82
$\mu_2 (in\ \phi)$	5.26	3.91	5.12	5.28	5.08	5.08	-	-	-	-	-	-
$\sigma_2 (in\ \phi)$	1.36	1.26	1.52	1.32	1.54	1.54	-	-	-	-	-	-

Table 2 – Main parameters of distribution obtained fitting selected TGSDs. p = fraction of the coarse populations; μ_1, μ_2 means of coarse- and fine-grained populations, respectively; σ_1, σ_2 standard deviations of means of coarse- and fine-grained populations, respectively. *juv*, *lith* and *crys* are juvenile, lithic and crystal component, respectively.

Table

Total grain size distribution of components of fallout deposits and implications for magma fragmentation mechanisms: examples from Campi Flegrei caldera (Italy)

Mele D.[1], Costa A.[2], Dellino P. [1], Sulpizio R.[1,3], Dioguardi F.[4], Isaia R.[5], Macedonio G.[5]

Supp. Figure 1

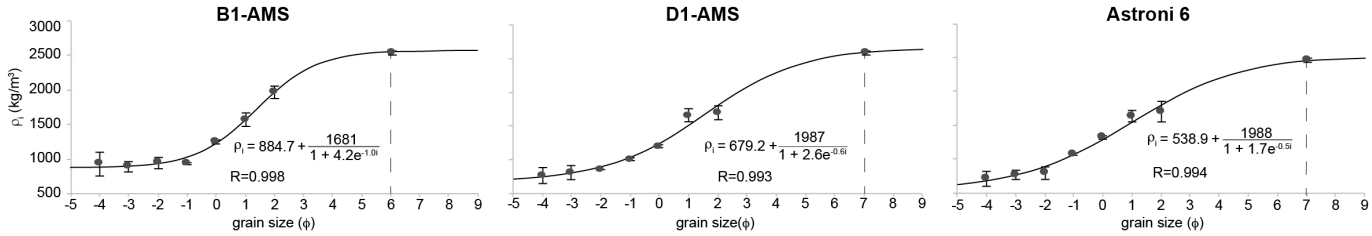

Supplementary material Figure 1. Size vs. density diagrams of juvenile component. The vertical dashed line shows the density value of dense rock equivalent.

Supp. Figure 2

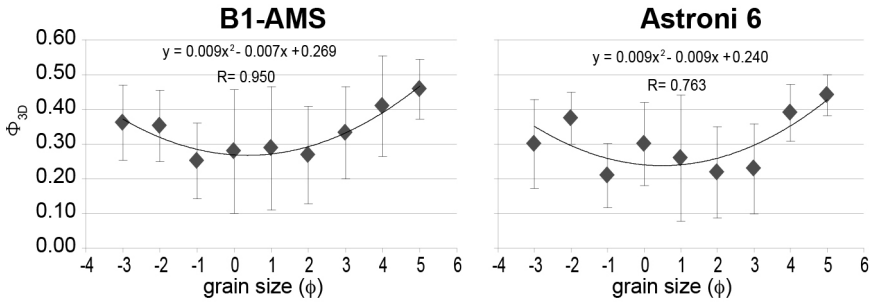

Supplementary material Figure 2. 3D sphericity vs. size diagram of pumices of B1 phase of Agnano-Monte Spina, and Astroni 6 eruptions (after Mele and Dioguardi 2018). 3D sphericity of pumices of D1 phase (Agnano Monte Spina eruption) was assumed equal to particles of B1 phase. Error bars for each grainsize are shown. The solid black line represents the best fit, of which correlation equations and coefficients are displayed.

Supp. Figure 3

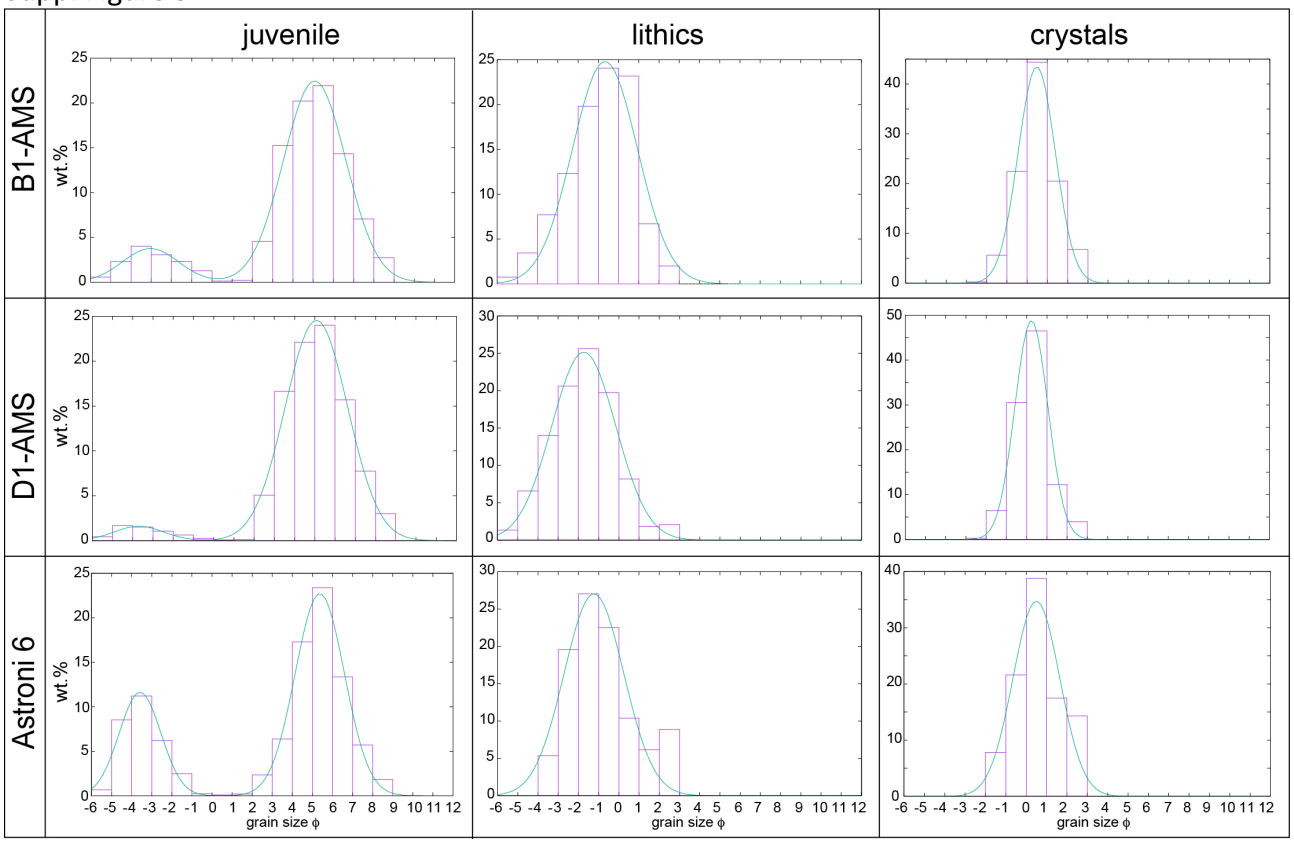

Supplementary material Figure 3. TGSD of juvenile, lithic, and crystal components. Lines show the coarse and fine sub-populations whose sum (full line) fit the observed distribution.